Heterogeneous SARS-CoV-2 kinetics due to variable timing and intensity of immune responses

Katherine Owens[1], Shadisadat Esmaeili-Wellman[1], and Joshua T. Schiffer[1,2]

1. Fred Hutchinson Cancer Center, Vaccine and Infectious Diseases Division
2. University of Washington, Department of Medicine

Abstract

The viral kinetics of documented SARS-CoV-2 infections exhibit a high degree of inter-individual variability. We identified six distinct viral shedding patterns, which differed according to peak viral load, duration, expansion rate and clearance rate, by clustering data from 810 infections in the National Basketball Association cohort. Omicron variant infections in previously vaccinated individuals generally led to lower cumulative shedding levels of SARS-CoV-2 than other scenarios. We then developed a mechanistic mathematical model that recapitulated 1510 observed viral trajectories, including viral rebound and cases of reinfection. Lower peak viral loads were explained by a more rapid and sustained transition of susceptible cells to a refractory state during infection, as well as an earlier and more potent late, cytolytic immune response. Our results suggest that viral elimination occurs more rapidly during omicron infection, following vaccination, and following re-infection due to enhanced innate and acquired immune responses. Because viral load has been linked with COVID-19 severity and transmission risk, our model provides a framework for understanding the wide range of observed SARS-CoV-2 infection outcomes.

Introduction

Even as the COVID-19 public health emergency status has lapsed in the United States, community levels of severe acute respiratory syndrome coronavirus 2 (SARS-CoV-2) remain significant (https://covid.cdc.gov/covid-data-tracker/#datatracker-home). SARS-CoV-2 immunity in the population is now highly heterogeneous due to varying degrees of prior infection and vaccination[1], and successive circulating SARS-CoV-2 variants of concern (VOC) with different immune evasion and infectivity properties continue to emerge and predominate. This has resulted in a wider variability of viral shedding patterns than those observed during infection with the ancestral strain in the early months of 2020[2,3]. Understanding the heterogeneous upper respiratory tract (URT) kinetics of SARS-CoV-2 enables informed design of health interventions such as testing, isolation, quarantine, and drug therapies.

Mathematical models are a vital tool to understand mechanisms underlying observed patterns of viral expansion and clearance[4–9] . To date, studies fitting SARS-CoV-2 dynamic models to viral load trajectories have estimated the timing of innate and acquired immune responses and predicted parameters of transmission, including super-spreader events[10–22]. These models facilitated estimates of key quantities such as expected duration of the infectious period and the timing of peak viral load relative to symptom onset[20,23–25]. They also provided a theoretical means for testing treatment regimens and predicted that treatment within 5 days of symptom onset would likely be associated with higher efficacy[11,22,24,26,27], an outcome that has since been verified in multiple clinical trials[28–30]. These models were also the first to suggest that viral rebound may occur in the context of early antiviral treatments[11].

However, early modeling studies only considered data from a small number of infected individuals[11,20,22–27,31–35], and often drew either entirely from previously uninfected and/or unvaccinated cohorts[13]. Another consistent limitation was that most available data did not capture early timepoints during the pre-symptomatic phase of infection. Model results are therefore not easily generalized to current SARS-CoV-2 conditions.

The National Basketball Association's (NBA) daily testing program occurred regardless of symptoms and identified 2,875 infections between June 2020 and January 2022, spanning the alpha, delta, and early omicron VOC waves, as well as the roll-out of vaccines and boosters. Hay et al. used a statistical approach to quantify the impact of immune history and variant on SARS-CoV-2 viral kinetics and infection rebound in this data set[36]. However, a more mechanistic modeling approach is required to understand observed kinetic variability in this cohort.

Here, we identify six distinct shedding patterns in the NBA cohort data. We then compare how well candidate models which extend the classical target-cell limited model previously published by Goyal et al.[11,22] and Ke at al.[20,23] recapitulate the longitudinal viral load data from 1510 sufficiently documented infections. After obtaining data-validated parameter estimates for each individual infection, we identify the factors underlying differing rates of viral expansion and clearance, peak viral loads, and duration of infection observed in the data. We use the model to

identify differences between the timing and intensity of the immune response during initial and re-infections and identify a potential explanation for viral rebound observed in the cohort.

Results

Viral shedding kinetics according to SARS-CoV-2 VOC.

We first analyzed viral kinetics observed in the cohort according to VOC. For pre-VOC, alpha, delta and omicron variants, we observed highly variable kinetics among cohort participants. Median values differed between variants, with omicron variant having slightly lower peak viral loads and earlier clearance, while delta had the highest peak viral loads and pre-VOC had the longest time to clearance (**Fig 1a-d**). A high proportion of the infections caused by omicron variants occurred in participants who had received either two or three vaccine doses, whereas pre-delta infections mostly occurred in unvaccinated individuals (**Fig 1e**).

The age structure of the NBA cohort differs significantly from the general population. Of the cases documented, 47% occurred in individuals under the age of 30, 42% occurred in individuals between the ages of 30 and 50, and only 12% occurred in individuals over the age of 50. Symptom status was noted for 59% of infections, of which 72% were symptomatic. The level of post-vaccination, pre-infection SARS-CoV-2 IgG was measured in 60% of infections. When stratifying patients into terciles, Hay et al. identified low antibody titers as less than 125 (arbitrary units [AU]/ml), mid-range titers as greater than 125 AU but less than 250 AU, and high titers as greater than 250 AU with the most infections occurring in the highest tertile. 17% of observed infections were reinfections of individuals followed longitudinally (**Fig 1f**).

Six distinct SARS-CoV-2 shedding patterns.

We identified a subset of infections in the NBA cohort as "well-documented" if they had at least 4 quantitative positive viral load measurements, and infection was documented through day 20 post-detection, or viral elimination was confirmed prior to 20 days post-detection with 2 sequential negative test results. This reduced the data set by about half to 810 well-documented infections. We then applied k-means clustering to the viral load data from the date of detection through 20 days after detection for this subset of infections, clustering the individual infections into 6 distinct viral shedding patterns (**Fig. 2a-c**) which differed according to time to viral elimination (**Fig. 2c,d**), viral area under the curve (**Fig. 2c,e**), peak viral load (**Fig. 2c,f**) and time to peak (**Fig. 2c,g**).

The first group had low peak viral loads and early median time to clearance (**Fig. 2a-g**). The second group had a slightly earlier and significantly higher peak than group 1, but similarly short duration (**Fig 2a-g**). The third group had a similar peak viral load compared to group 2, but with a longer time to peak viral load due to a slower expansion rate, and later clearance resulting in a larger area under the $\log_{10}$ viral load curve (**Fig 2a-g**). The fourth group had the fastest expansion rate, reaching a high, early peak viral load, but maintaining similar median time to clearance as group 3 (**Fig 2a-g**). The fifth group has the slowest expansion rate, taking the longest time to reach the second lowest peak viral load and had the longest median time to clearance among the groups (**Fig 2a-g**). In contrast with the prolonged low-level shedding of group 5, the sixth group had high peak viral and a long shedding duration resulting in the highest area under the $\log_{10}$ viral load curve (**Fig 2a-g**).

The proportion of cases that fell into each dynamic group varied when we stratified by several characteristics included in the data set. The dynamic groups with highest AUC, groups 5 and 6, made up around 39% of the infections in the 50 plus age group, whereas only around 20% of infections in the under 30 group fall into the high AUC groups (**Fig. 2h**). Among confirmed asymptomatic infections, 33% of cases fell into group 1, defined by low peak and early time to clearance, relative to only 18% of confirmed symptomatic cases (**Fig. 2i**). The prevalence of high AUC shedding patterns was also higher for SARS-CoV-2 variants from earlier in the pandemic, making up 61% of pre-VOC infections, 26% of delta infections, and only 8% of omicron infections (**Fig. 2j**). Amongst unvaccinated individuals, high AUC infection patterns were over 5 times as common as in fully vaccinated individuals—that is 58% of infections in unvaccinated individuals fell into groups 5 and 6, compared with 11% and 10% of infections for those whose most recent SARS-CoV-2 vaccine was their second dose or booster respectively (**Fig. 2k**).

Mathematical model fit to viral loads from 1510 SARS-CoV-2 infections.

To identify factors underlying the varied viral shedding patterns in the NBA cohort, we developed competing mechanistic mathematical models of viral and immune dynamics and selected the best model according to data fitting criteria. This model adapts previously published ordinary differential equations models for within-host SARS-CoV-2 infections by combining elements introduced by Goyal et al.[11,22] and Ke et al.[20,23] . Mechanistic assumptions inherent to many pre-existing viral dynamic models include a viral load dependent infectivity, viral production by infected cells, a limited number of susceptible cells and a pre-production eclipse phase for infected cells. Other assumptions that optimized model fit included conversion of susceptible cells to an infection-refractory state dependent on the number of infected cells (presumably representing innate responses to infection), linear reversion of these refractory cells to a susceptible state, density-dependent death of infected cells as a proxy for an intensifying cytolytic innate response to a higher burden of infection, and a delayed cytolytic acquired immune response (**Fig. 3a; Materials and Methods**).

We used a nonlinear, mixed-effects framework to estimate model parameters for the 1510 infections documented in 1442 individuals in the NBA cohort that had at least 4 quantitative viral load measurements (**Materials and Methods**). We first used a representative subsample of these infections to compare model fits for the full model, illustrated in **Fig. 3a** and written out in Eq. 1, as well as reasonable simplifications of the model, in which one or more immune mechanism was removed (**Materials and Methods, Table S1**). Under model selection criteria that balance model simplicity with accuracy, the best model to explain the NBA data from among those we considered was the full model without any terms removed. We then refit the best model to all 1510 infections. It is possible that a more complex model could describe the data even better; however, the fits that we achieve with this model were highly accurate (**Fig. 3b, Fig. S7**).

Differences in timing and intensity of immune response as an explanation for heterogeneous shedding patterns.

We next sought to explore possible virologic and immunologic mechanistic explanations for different observed viral shedding patterns. For relevant model quantities, we calculated the

mean value within each dynamic group at each time point and a 95% confidence interval assuming normally distributed values. Viral loads projected by the model for each group (**Fig. 4a**) resembled those from the actual data (**Fig 2c**). Quantitative kinetic features extracted from model predictions including peak viral load, time to peak, viral area under the curve and shedding kinetic group also agreed well with those extracted from the data (**Fig S1a-f**). Dynamic groups with later peak viral loads (G3, G5, G6) had a slower transition of susceptible cells to a refractory state relative to groups with earlier peak viral loads (G1, G2, G4) (**Fig 4b**). Furthermore, the group with the lowest peak viral loads and earliest time to clearance, G1, had a markedly higher proportion of cells entering the refractory state, and the key distinction between prolonged shedders with low peak viral load (G5) and those with high viral load (G6) was also the proportion of refractory target cells (**Fig 4b**). The magnitude of the early cytolytic immune response was markedly higher for group 2 compared to the other 5 groups, which had high peak viral loads but early clearance (**Fig 4c**). The relative ordering of the groups in terms of mean time to acquired immune onset (**Fig 4d**) mirrored the ordering of median clearance time for the 5 groups observed in the data (**Fig 2d**). The earliest late immune responses were also the most intense.

We also compared the value of model parameters across the six dynamic groups (**Fig S2**). The per-infected cell conversion rate of susceptible to refractory cells, ϕ, was much more rapid for group 1 relative to the other groups, contributing to lower, earlier peak viral loads (**Fig S2b**). In contrast, groups 3, 5 and 6 reached peak viral load later due to lower product of viral infectivity, β, and viral production rate, π (**S2c-e**). Group 2 had the most rapid clearance of the virus due to an elevated value of early clearance of infected cells, δ, in comparison to the other groups (**S2i**). The high peaks observed in groups 4 and 6 were driven by a higher viral production rate, π, and lower rate of conversion of target cells to a refractory state, ϕ, resulting in the highest ratio between these two values (**S2b,c,f**). Conversely, group 5 had a lower ratio between these two parameter values (**S2f**), and thus a low peak despite prolonged shedding. This prolonged shedding observed in groups 5 and 6 resulted from a significantly later onset of acquired immunity compared to the other groups (**S2k**). Overall, these results suggest a complex interplay of viral and immune features dictate how individual infections differ according to peak viral load, viral expansion rate, viral clearance rate, and duration of shedding.

As a sensitivity analysis, we calculated the Pearson correlation coefficient between individual estimates for each model parameter and 3 viral kinetic quantities predicted by the mathematical model: log of peak viral load, time to peak viral load, and shedding duration (**Fig. 4e-g**). The peak viral load correlated strongly with viral production rate, π, and had a strong inverse correlation with the rate of conversion of susceptible cells to a refractory state, ϕ (**Fig. 4e**). A linear model mapping $\log(\pi/\phi)$ to log peak viral load explained a large amount of variability (**Fig. 4h**). The timing of peak viral load inversely correlated strongly with π, β, and ϕ (**Fig. 4f**). We fit an exponential model for time to peak viral load relative to infection as a function of $\log_{10}(\beta\pi)$, which again explained a large amount of variability, $R^2 = 0.9$ (**Fig. 4i**). Finally, the shedding duration correlated most strongly with the time of onset of acquired immunity in the model, τ (**Fig. 4g, j**).

We examined the correlations between estimated model parameters and found several significant patterns (**Fig S3**). Viral infectivity, β, had a positive correlation with the rate at which susceptible cells were driven to a refractory state, ϕ. The refractory conversion rate also had a strong negative correlation with the rate of reversion to susceptibility, ρ, and the intensity of early cytolytic immune pressure, δ. These two parameters, ρ and δ, were strongly positively correlated. There was also a strong correlation between the intensity of early cytolytic immune pressure, δ, and late cytolytic immune pressure, m.

Lower peak viral load and earlier clearance during reinfection with omicron due to more effective early immune responses and more rapid late responses.

The NBA cohort data set documented initial infection and reinfection in 67 individuals. Five examples, along with corresponding model fits, are plotted in **Fig. 5a**. Plots of the viral load during infections in all 67 individuals are included **Fig. S4**. Of the first infections, 52 were caused by a pre-delta variant and 15 by delta. For all individuals, the second infection was caused by an omicron variant. The mean peak viral load documented for a re-infection was 0.5 log lower than the mean for first infections. Though there was a slight negative correlation between peak viral load during the first infection and that of the second infection (**Fig. 5b**), the relationship was not statistically significant ($r_{pearson} = -0.18,\ p = 0.15$). The median time to clearance for reinfections was 7.5 days after detection compared with 11 days after detection for first infections (**Fig. 5c**).

When comparing model parameter values for first versus second infections, we observed that three were significantly different (**Fig. 5d**). Reinfections had higher infectivity, β, but lower viral replication rate, π. This may reflect differences between omicron and earlier SARS-CoV-2 variants, as well as early immune responses which contribute to lower peak viral loads. The timing of the acquired immune response, τ, was also earlier, during reinfection suggesting more rapid activation of immune memory. Model projections recapitulated viral load patterns observed in the data (**Fig 5e**). We plotted the immune terms from the model simulations for the two groups as well, and reinfection appeared to result in both more refractory cells (**Fig 5f**) and a more robust early immune response **(Fig 5g)**. More significantly, the acquired immune response initiated sooner and at a higher magnitude for reinfection (**Fig 5h**).

Waning early immune response and strong initial clearance of infected cells as a cause of off-therapy viral rebound.

Recent studies have shown that viral rebound during the natural course of untreated SARS-CoV-2 infection is relatively common, occurring in over 10% of cases by some estimates[37] (https://www.fda.gov/media/166197/download). In their analysis of the NBA cohort, Hay et al. flagged 40 out of 1334 cases (3%) as rebound, defined by a non-monotonic sequence of test results[36]. As their most inclusive definition of rebound, they identified cases that achieved an initial clearance of at least 2 days with cycle threshold greater than or equal to 30, followed by at least 2 days with cycle threshold < 30.

We examined model simulations of infections in the NBA cohort, and defined infections as rebound if there were 2 or more peaks with height > 3 $\log_{10}$ RNA copies/ml and prominence > 1

$\log_{10}$ RNA copies/ml. Here we defined prominence as the height above the preceding local minima, as illustrated in (**Fig. 6a**). With this viral load-based criteria, we identified 9.0% of the 1510 cases as rebound. These cases are marked with an "R" and included first in **Fig S7**. Note that we were unable to connect viral rebound to recrudescence of COVID-19 symptoms because we do not have daily reports of symptom status.

Considering the mean immune responses for these two groups, we observed several key differences. In cases of rebound (**Fig 6b**), susceptible cells were lost more rapidly initially, but they were then replenished more rapidly from the refractory compartment (**Fig. 6c-d**). This allowed for a second surge of viral production, which had been reduced by fast early clearance of infected cells (**Fig 6e**). The delayed onset of the late acquired immune response also allowed sufficient time for this to occur before the infection was ultimately cleared (**Fig 6e**). Cases with rebound had higher viral production rates, π, which is crucial for growth of the viral population even with a reduced number of target cells. Rebound cases also had a higher early immune clearance rate, δ, which was necessary to achieve the rapid initial clearance of infected cells that preserves susceptible cells. Crucially, rebound cases also had a significantly higher reversion rate, ρ, to account for replenishment of susceptible cells after the first viral peak. To compensate for the higher viral production rate, the viral rebound group also had a more intense late immune killing rate, m (**Fig 6g**). Rebound cases could also be further stratified by timing of the second peak with slightly different mechanistic underpinnings (**Fig. S5)**.

Discussion

Viral kinetics are vital to understanding the pathogenesis of infection and, ultimately, to optimizing therapies. Here we use a remarkable cohort from the NBA, which is unique both for its size and because it captures early pre-symptomatic timepoints during infection, to describe the increasing variability in viral load patterns observed in SARS-CoV-2 infected people. We observe that with a general increase in population level immunity due to prior infection and vaccination, peak viral load is often lower and earlier with more rapid elimination of virus.

Our mathematical model identifies testable mechanistic hypotheses for these observed differences. We first predict that low peak viral loads are associated with lower viral production within infected cells and lower viral infectivity. Moreover, for viral loads that also peak early (observed in group 1), the model predicts a rapid conversion of susceptible cells to a refractory state. Both effects are compatible with data observed in animal models and *in vitro* models describing effects of interferon effects which limit the extent of viral replication and protect uninfected cells from viral entry[38–42]. Appropriate follow up experiments to validate this prediction would include local sampling of nasal cytokines and other mediators of local immunity during critical early timepoints of infection as has been done in humans for other respiratory viral infections[43].

The magnitude of the early cytolytic immune response, which wanes as the number of infected cells and viral load declines following peak, appears to predict an earlier and more effective late sustained immune response. In our model, we assumed this response does not dissipate with decrease in virus, so we hypothesize that most of the late response is acquired and due to either expanding T cell or antibody levels. Prior work suggested that during primary infection, plasma SARS-CoV-2 IgG levels rise too late to explain reduction in viral load[44]. However, the study was performed in an immunologically naïve cohort and needs to be reassessed in the current infection environment[45,46]. T cell mediated killing of infected cells may also assist in elimination of infected cells during infection[45,47].

Our results suggest that the early/innate response is coupled to the effectiveness of the late acquired response. The mechanisms underlying this observation are unclear. One possibility is that a higher density of tissue resident NK cells, B cells and T cells may exist after first infection and vaccination. In other viral infections, it has been observed that an increase in pre-infection tissue resident T cells predicts earlier initiation of a local innate and acquired response due to early antigen recognition[48,49]. Alternatively, early binding and neutralization of viruses due to pre-existing antibodies may lower infectivity. Correlation between effective early and late responses was clearly observed during re-infection in individuals who had two infections during the observation window, suggesting that an early component of acquired immune pressure may indeed be important. These model predictions merit experimental follow up.

Unfortunately, we are not able to link the heterogenous virologic patterns observed in the NBA cohort with severity of symptoms or future development of post-acute sequelae of SARS-CoV-2 infection as this data was not available. For multiple other viruses, viral loads have been

identified as relevant correlates of disease[50–53], and late SARS-CoV-2 viral loads have been linked with severity of infection among hospitalized people[54,55]. During clinical trials, reductions in nasal viral load due to monoclonal antibodies, nirmatrelvir / ritonavir, and molnupiravir correlated with very large reductions in the incidence of hospitalization and death[28,29]. Yet, early remdesivir which had a large clinical benefit was associated with no viral reduction in nasal passage[30], highlighting that key viral load surrogates may be in the lung rather than nasal passages[22]. In addition, because early and peak viral load measurements are so rarely obtained during COVID-19 infection, the clinical importance of these values remain unknown.

Several further limitations of this work are important to highlight. An issue that is universal to the field is that our model does not capture anatomic compartmentalization of viral shedding. A previous model demonstrated in non-human primates that SARS-CoV-2 kinetics in the lung differ in subtle but important ways from those in the upper airways, and that these differences are particularly significant in the context of antiviral therapy[22]. It is likely that our subgroups of shedding may cluster differently if we had access to serial whole lung viral loads. The re-seeding of infection in the nose from the lungs or vice versa may also provide alternative explanations for the dynamics observed in this data set, particularly viral rebound. Unfortunately, such detailed studies are not available in any human cohort. Studies using saliva do suggest slightly different kinetics than those from nasal swabs[56], but it is doubtful that saliva captures total viral load in the lung.

Another issue shared by all mathematical models in the field is the lack of sufficiently granular, tissue-based immune data to precisely model the innate and acquired immune response. Rather, our model uses several terms to capture the timing and intensity of what is likely to be a complex, multi-component response. Specifically, we use a density dependent killing term to capture early immunity: this assumes no memory and enhanced killing rates decrease as viral load decreases making this response most compatible with innate immunity. As with multiple other respiratory virus models and based on experimental data showing that interferon-alpha protects cells from infection, we also assume that infection temporarily makes susceptible cells refractory to viral entry[20–22,39,42]. Finally, we assume a late, sustained immune response that varies by intensity and timing, compatible with an acquired memory response.

A final limitation shared by all intra-host SARS-CoV-2 models in humans is that we are not able to measure potentially important initial conditions of infection, including viral inoculum and the number of immune cells within a relevant spatial microenvironment of infection. Thus, though we estimate the viral inoculum for each individual infection, the model may over ascribe observed differences in observed viral load trajectories to differences in immune responses rather than exposure viral load.

In summary, we identify distinct shedding patterns in adults with SARS-CoV-2 infection, with shorter, lower viral load infection more commonly observed in persons with omicron infection, prior vaccination, and recent prior infection. The mechanistic predictors of rapidly contained infection are more rapid conversion of susceptible cells to a refractory state along with more rapid and intense late cytolytic immune responses.

Materials and Methods

Study Overview.

We analyzed SARS-CoV-2 viral load data collected during untreated infections in the NBA cohort. We clustered this data into 6 dynamic groups, which are statistically different in terms of peak viral load, time to peak viral load, area under the viral load curve, and time to clearance. We developed a family of candidate ordinary differential equation (ODE) mathematical models inspired by previous models in the field. We then used model selection theory to compare multiple instances of these models and determine which version the data supported most strongly. With a validated model of SARS-CoV-2 infection, we examined which parameter values differ to explain the varying viral shedding patterns observed in the six dynamic groups. We also used this approach to explain the differing dynamics of first and second infections captured in the NBA cohort, and to explain the mechanisms underlying viral rebound.

Data Pre-processing.

We used data from the NBA cohort previously published by Hay et al.[36] . The group documented 2875 individual SARS-CoV-2 infections in 2678 people through frequent quantitative PCR testing. First, we filtered this data to include only infections with at least 4 positive quantitative samples to retain only those individuals with adequate viral dynamics data for model fitting. This yielded 1510 infections in 1442 individuals, of which 177 were caused by a pre-VOC variant, 46 by alpha, 163 by delta, and 1124 by omicron (**Fig. 1a**). We further identified a "well-documented" subset of these infections by filtering for infections that included test results through 20 days after detection or infections with confirmed elimination of virus prior to day 20 (two consecutive negative tests). This well-documented group consisted of 810 individual infections in 768 people. We further filtered the well-documented group to include only those that had a negative test result within 2 days of detection, yielding 266 cases with both early detection and 3 weeks of documentation.

Quantitative Features of Viral Dynamics

To convert cycle threshold (Ct) values to viral genome equivalents, we first averaged Ct1 and Ct2 for each individual and then applied equation S2 from Kissler et al.[57] That is,

$$\log_{10}([RNA]) = (Ct_{avg} - 40.93733)/(-3.60971) + \log_{10}(250),$$

where the concentration of viral RNA is in copies/ml. Throughout the manuscript, we refer to this as $\log_{10}$ viral load.

We calculated the peak viral load for a given infection as the maximum measured $\log_{10}$ viral load over all quantitative data points. We calculated the area under the $\log_{10}$ viral load curve from the date of detection through the last quantitative measure of viral load, linearly imputing missing values between data points. Note that this quantity is likely an underestimate, particularly for individuals without confirmed clearance. We calculated the median time to clearance by identifying when the cumulative incidence curve for clearance of the virus crossed 50%. The cumulative incidence curve is the inverse of the Kaplan-Meier curve for survival of the

virus. The Kaplan-Meier curve, KM, and confidence interval was computed using the Python package scikit-survival 0.21.0 (https://scikit-survival.readthedocs.io/en/stable/). The cumulative incidence curve is then 1-KM.

Data Clustering

We clustered the 810 well-documented infections into 6 dynamic groups using k-means clustering as implemented in the Python package scikit-learn 1.2.2 (https://scikit-learn.org/stable/modules/generated/sklearn.cluster.KMeans.html). To construct a set of features for clustering, we considered a time window from the day infection was detected through 20 days after detection. If any daily measurements were missing between recorded test values, we imputed the missing measurements linearly. If the last test date for an individual was prior to day 20, so there were missing daily measurements after the last test, we appended negative test values to reach 20 days (**Fig S6a**). This only occurred for infections for which clearance was confirmed with 2 consecutive negative tests, since we were used only well-documented infections. We used these 21 daily test results as the features for k-means clustering.

To select these hyperparameters for the k-means clustering, we tested values of k from 2 to 20 for three possible interpolation methods, linear, quadratic, or cubic spline, and two possible surveillance periods, 13 or 20 days (2 or 3 weeks) post detection. **Fig. S6b** shows the mean within-cluster sum of squared error for these different hyperparameter settings. Across the different modes of interpolation and durations of surveillance, linear interpolation up to 20 days post detection had the lowest error. Based on the location of the "elbow" in the plots, we chose to proceed with k = 6 clusters. Using k < 6 results in less distinctive behaviors between the groups, while using more clusters resulted in some non-interpretable cluster centers (**Fig. S6c).**

Mathematical Model of SARS-CoV-2 Dynamics

We considered several possible ordinary differential equations models for SARS-CoV-2 infection dynamics. The full model tracks the number of target cells that are susceptible to infection (S), target cells that are refractory to infection (R), infected cells in an eclipse phase (I_E), infected cells actively producing virus (I_P), and SARS-CoV-2 virions (V). Susceptible cells are infected at rate βSV, and become refractory at rate $\phi I_p S$. Refractory cells revert to a susceptible state at rate ρR. When cells are first infected, they enter an eclipse phase, from which they transition to a state of producing virus at rate k. Productively infected cells are cleared at rate δI^{h+1}, where the dependence on infected cells reflects an innate immune response with no memory. When the duration of infection surpasses time τ, the clearance rate of infected cells increases by mI, capturing the delayed onset of a cytolytic acquired immune response with memory. Productively infected cells produce virus at rate π, and free virions are cleared at rate γV. Under these assumptions, the model has the form:

$$\frac{dS}{dt} = -\beta SV - \phi I_P S + \rho R \qquad (1a)$$

$$\frac{dR}{dt} = \phi I_P S - \rho R \qquad (1b)$$

$$\frac{dI_E}{dt} = \beta SV - kI_E \quad (1c)$$

$$\frac{dI_P}{dt} = kI_E - \delta I_P^h I_P - m(t)I_P \quad (1d)$$

$$\frac{dV}{dt} = \pi I_P - \gamma V \quad (1e)$$

$$\text{where} \begin{cases} m(t) = 0 & t < \tau \\ m(t) = m & t \geq \tau. \end{cases} \quad (1f)$$

As initial conditions, we set $(S_0, R_0, I_{E0}, I_{P0}, V_0) = (1 \times 10^7, 0, 0, 0, V_0)$. Previous models of SARS-CoV-2 infection in the nasal compartment have used an initial value of $10^7 - 10^8$ susceptible cells, based on estimates that 2-20% of epithelial cells in the upper respiratory tract display the ACE 2 receptor[58,59,60]. We assumed that the initial number of refractory cells is zero, i.e. because the early immune response is inactive prior to infection. We initiated simulations with zero infected cells, so $I_{E0} = I_{P0} = 0$, and a small viral inoculum to reflect the tight bottleneck that transmission places on viral replication. The number of virions present at the outset of infection was assumed to be below the limit of detection, but the precise inoculum varies for individuals. We also estimated the onset of infection relative to detection, t_0. In the NBA cohort, the mean time of symptom onset was the date of detection, so t_0 is correlated with the incubation period of SARS-CoV-2. With this in mind, we restricted estimates of t_0 to fall between 0 and 20 days based on a 2022 review by Wu et al., which reported that across 142 studies of SARS-CoV-2 infection, the incubation period ranged from 1.80 to 18.87 days[61].

To maintain identifiability, we fixed two parameter values, setting the rate of viral production onset to be $k = 4$ in accordance with Ke at al.[23] and the rate of clearance of free virions to be $\gamma = 15$ in accordance with Goyal et al.[11]

Model Fitting and Selection.

We fit the model in Eq. 1 to the well-documented, early detection subset of the NBA cohort data set, as well as simpler versions that eliminate one or more immune components and/or the eclipse phase, using a non-linear mixed effect approach[62]. With this approach, a viral load measurement from individual i at time point k is modeled as $\log_{10}(y_{ik}) = f_V(t_{ik}, \theta_i) + \epsilon$, where f_V represents the solution of the ODE model for the state variable describing the virus, θ_i is the parameter vector for individual i, and $\epsilon \sim N(0, \sigma^2)$ is the measurement error for the $\log_{10}$-transformed viral load data. We fixed $\sigma^2 = 0.5$ when assessing model fits, so that any differences in likelihood of the full model occur due to a change in agreement between model simulations and data rather than an increase in the estimated magnitude of the measurement error.

For model selection, we worked with the data from 266 infections with early detection and at least 3 weeks of follow-up or clearance. For viral load observations below the lower limit of quantification or marked as "assumed negative", we used the probabilistic model that Monolix

software provides for left-censored data (https://monolix.lixoft.com/censoreddata/). The candidate models that we considered are listed in the supplementary material (**Table S1**). For each candidate model, we used the Stochastic Approximation of the Expectation Maximization (SAEM) algorithm embedded in the Monolix software to obtain the Maximum Likelihood Estimation (MLE) of the vector of fixed effects, θ_{pop}, and the MLE of the vector of standard deviations of the random effects, σ_θ, for the model parameters $\beta, \pi, \phi, \rho, \delta, h, \tau, m$, the delay between infection and data of detection, t_0, and the initial viral inoculum, V_0 (https://monolix.lixoft.com/tasks/population-parameter-estimation-using-saem/). For parameter values we considered a lognormal distribution across the population. For the estimated initial conditions, we used a logit distribution to be able to enforce that they fall within reasonable ranges. The delay between infection and detection, t_0, was assumed to follow a logit distribution with minimum 0 and maximum 20 days. The viral inoculum was assumed to follow a logit distribution with minimum 1 and maximum 250.

We ran the SAEM algorithm six times for each model using randomly selected initial values for the estimated parameters. Using the parameter set with the highest likelihood, we computed the Akaike Information Criterion (AIC) for each model. Recall that $AIC = -2\max(\log \mathcal{L}) + 2m$ where $\mathcal{L}$ is the likelihood that the data was generated by this model with these parameter values and m is the number of model parameters. Hence smaller AIC scores indicate that a model is statistically more likely to explain the data. The model with the smallest AIC score in the initial model selection phase was the full model with all immune components included and an eclipse phase. All AIC scores are recorded in **Table S1**.

For the best fitting model, there were significant correlations between the random effects of model parameters $\beta, \pi, \phi, \rho, \delta, m$, and τ as well as the date of infection relative to detection, t_0. We allowed for linear correlations between these parameters in the model (https://monolix.lixoft.com/statistical-model/individual-model/individualdistribution/). This further improved the AIC score of the model by 161 points. AIC scores comparing alternative correlation structures are recorded in **Table S2**. The correlation structure of the final set of parameter estimates is shown in **Figure S3**.

Once the final model was selected, we ran the SAEM algorithm in Monolix to estimate parameters for all 1510 infections. The resulting estimated parameter values were used for all model-based results. Population parameter values are included in **Table S3** and individual model fits are shown in **Figure S7**. Estimated individual parameter values are accessible on github at https://github.com/lacyk3/SARS-CoV-2Kinetics.

Data availability

The data analyzed in this work was previously published by Hay et al. and is available on github at https://github.com/gradlab/SC2-kinetics-immune-history.

Acknowledgements

We thank Yonatan Grad, Stephen Kissler, and the members of the NBA cohort for making this data available. We also thank Dan Reeves and Liz Duke for their helpful advice regarding figures. This work was supported by National Institutes of Health (NIH) grants R01AI169427 & R01AI121129.

References

1. Bobrovitz, N. *et al.* Protective effectiveness of previous SARS-CoV-2 infection and hybrid immunity against the omicron variant and severe disease: a systematic review and meta-regression. *Lancet Infect Dis* **23**, 556–567 (2023).
2. van Kampen, J. J. A. *et al.* Duration and key determinants of infectious virus shedding in hospitalized patients with coronavirus disease-2019 (COVID-19). *Nat Commun* **12**, 267 (2021).
3. Wu, Y. *et al.* Duration of viable virus shedding and polymerase chain reaction positivity of the SARS-CoV-2 Omicron variant in the upper respiratory tract: a systematic review and meta-analysis. *Int J Infect Dis* **129**, 228–235 (2023).
4. Schiffer, J. T. *et al.* Mathematical modeling of herpes simplex virus-2 suppression with pritelivir predicts trial outcomes. *Sci Transl Med* **8**, (2016).
5. Goyal, A., Liao, L. E. & Perelson, A. S. Within-host mathematical models of hepatitis B virus infection: Past, present, and future. *Current Opinion in Systems Biology* vol. 18 27–35 Preprint at https://doi.org/10.1016/j.coisb.2019.10.003 (2019).
6. Nguyen, V. K. & Hernandez-Vargas, E. A. Windows of opportunity for Ebola virus infection treatment and vaccination. *Sci Rep* **7**, (2017).
7. Duke, E. R., Boshier, F. A. T., Boeckh, M., Schiffer, J. T. & Cardozo-Ojeda, E. F. Mathematical modeling of within-host, untreated, cytomegalovirus infection dynamics after allogeneic transplantation. *Viruses* **13**, (2021).
8. Huynh, G. T. & Adler, F. R. Alternating Host Cell Tropism Shapes the Persistence, Evolution and Coexistence of Epstein-Barr Virus Infections in Human. *Bull Math Biol* **73**, 1754–1773 (2011).
9. Perelson, A. S., Neumann, A. U., Markowitz, M., Leonard, J. M. & Ho, D. D. HIV-1 Dynamics in Vivo: Virion Clearance Rate, Infected Cell Life-Span, and Viral Generation Time. *Science (1979)* **271**, 1582–1586 (1996).
10. Goyal, A., Reeves, D. B. & Schiffer, J. T. Multi-scale modelling reveals that early super-spreader events are a likely contributor to novel variant predominance. *J R Soc Interface* **19**, 20210811 (2022).
11. Goyal, A., Fabian Cardozo-Ojeda, E. & Schiffer, J. T. *Potency and timing of antiviral therapy as determinants of duration of SARS-CoV-2 shedding and intensity of inflammatory response*. *Sci. Adv* vol. 6 https://www.science.org (2020).
12. Goyal, A., Reeves, D. B., Cardozo-Ojeda, E. F., Schiffer, J. T. & Mayer, B. T. Viral load and contact heterogeneity predict SARS-CoV-2 transmission and super-spreading events. *Elife* **10**, (2021).
13. Néant, N. *et al.* Modeling SARS-CoV-2 viral kinetics and association with mortality in hospitalized patients from the French COVID cohort. *PNAS* **118**, (2023).
14. Marc, A. *et al.* Quantifying the relationship between SARS-CoV-2 viral load and infectiousness. *Elife* **10**, (2021).
15. Perelson, A. S. & Ke, R. Mechanistic Modeling of SARS-CoV-2 and Other Infectious Diseases and the Effects of Therapeutics. *Clin Pharmacol Ther* **109**, 829–840 (2021).
16. Elie, B. *et al.* Variant-specific SARS-CoV-2 within-host kinetics. *J Med Virol* **94**, 3625–3633 (2022).

17. Ejima, K. *et al.* Estimation of timing of infection from longitudinal SARS-CoV-2 viral load data: mathematical modelling study. *BMC Infect Dis* **22**, 656 (2022).
18. Ohashi, H. *et al.* Different efficacies of neutralizing antibodies and antiviral drugs on SARS-CoV-2 Omicron subvariants, BA.1 and BA.2. *Antiviral Res* **205**, 105372 (2022).
19. Kim, K. S. *et al.* A quantitative model used to compare within-host SARS-CoV-2, MERS-CoV, and SARS-CoV dynamics provides insights into the pathogenesis and treatment of SARS-CoV-2. *PLoS Biol* **19**, e3001128 (2021).
20. Ke, R. *et al.* Daily longitudinal sampling of SARS-CoV-2 infection reveals substantial heterogeneity in infectiousness. *Nat Microbiol* **7**, 640–652 (2022).
21. Ke, R., Zitzmann, C., Ho, D. D., Ribeiro, R. M. & Perelson, A. S. In vivo kinetics of SARS-CoV-2 infection and its relationship with a person's infectiousness. *Proceedings of the National Academy of Sciences* **118**, (2021).
22. Goyal, A., Duke, E. R., Cardozo-Ojeda, E. F. & Schiffer, J. T. Modeling explains prolonged SARS-CoV-2 nasal shedding relative to lung shedding in remdesivir-treated rhesus macaques. *iScience* **25**, (2022).
23. Ruian Ke, Carolin Zitzmann, David D. Hoc, Ruy M. Ribeiro & Alan S. Perelson. In vivo kinetics of SARS-CoV-2 infection and its relationship with a person's infectiousness. (2021) doi:https://doi.org/10.1073/pnas.2111477118.
24. Jeong, Y. D. *et al.* Revisiting the guidelines for ending isolation for covid-19 patients. *Elife* **10**, (2021).
25. Heitzman-Breen, N. & Ciupe, S. M. Modeling within-host and aerosol dynamics of SARS-CoV-2: The relationship with infectiousness. *PLoS Comput Biol* **18**, (2022).
26. Iwanami, S. *et al.* Detection of significant antiviral drug effects on COVID-19 with reasonable sample sizes in randomized controlled trials: A modeling study. *PLoS Med* **18**, (2021).
27. Gonçalves, A. *et al.* Timing of Antiviral Treatment Initiation is Critical to Reduce SARS-CoV-2 Viral Load. *CPT Pharmacometrics Syst Pharmacol* **9**, 509–514 (2020).
28. Hammond, J. *et al.* Oral Nirmatrelvir for High-Risk, Nonhospitalized Adults with Covid-19. *New England Journal of Medicine* **386**, 1397–1408 (2022).
29. Jayk Bernal, A. *et al.* Molnupiravir for Oral Treatment of Covid-19 in Nonhospitalized Patients. *New England Journal of Medicine* **386**, 509–520 (2022).
30. Gottlieb, R. L. *et al.* Early Remdesivir to Prevent Progression to Severe Covid-19 in Outpatients. *N Engl J Med* **386**, 305–315 (2022).
31. Kissler, S. M. *et al.* Viral dynamics of acute SARS-CoV-2 infection and applications to diagnostic and public health strategies. *PLoS Biol* **19**, (2021).
32. Jenner, A. L. *et al.* COVID-19 virtual patient cohort suggests immune mechanisms driving disease outcomes. *PLoS Pathog* **17**, (2021).
33. Kim, K. S. *et al.* A quantitative model used to compare within-host SARS-CoV-2, MERS-CoV, and SARS-CoV dynamics provides insights into the pathogenesis and treatment of SARS-CoV-2. *PLoS Biol* **19**, e3001128 (2021).
34. Grebennikov, D. *et al.* Predicting the Kinetic Coordination of Immune Response Dynamics in SARS-CoV-2 Infection: Implications for Disease Pathogenesis. *Mathematics* **10**, (2022).
35. Gonçalves, A. *et al.* SARS-CoV-2 viral dynamics in non-human primates. *PLoS Comput Biol* **17**, (2021).

36. Hay, J. A. *et al.* Quantifying the impact of immune history and variant on SARS-CoV-2 viral kinetics and infection rebound: A retrospective cohort study. *Elife* **11**, (2022).
37. Deo, R. *et al.* Viral and Symptom Rebound in Untreated COVID-19 Infection. *medRxiv* (2022) doi:10.1101/2022.08.01.22278278.
38. Chong, Z. *et al.* Nasally delivered interferon-λ protects mice against infection by SARS-CoV-2 variants including Omicron. *Cell Rep* **39**, 110799 (2022).
39. Sa Ribero, M., Jouvenet, N., Dreux, M. & Nisole, S. Interplay between SARS-CoV-2 and the type I interferon response. *PLoS Pathog* **16**, e1008737 (2020).
40. Schroeder, S. *et al.* Interferon antagonism by SARS-CoV-2: a functional study using reverse genetics. *Lancet Microbe* **2**, e210–e218 (2021).
41. Blanco-Melo, D. *et al.* Imbalanced Host Response to SARS-CoV-2 Drives Development of COVID-19. *Cell* **181**, 1036-1045.e9 (2020).
42. Vanderheiden, A. *et al.* Type I and Type III Interferons Restrict SARS-CoV-2 Infection of Human Airway Epithelial Cultures. *J Virol* **94**, (2020).
43. Waghmare, A. *et al.* Reliability of Self-Sampling for Accurate Assessment of Respiratory Virus Viral and Immunologic Kinetics. *J Infect Dis* **226**, 278–286 (2022).
44. Yang, S., Jerome, K. R., Greninger, A. L., Schiffer, J. T. & Goyal, A. Endogenously Produced SARS-CoV-2 Specific IgG Antibodies May Have a Limited Impact on Clearing Nasal Shedding of Virus during Primary Infection in Humans. *Viruses* **13**, (2021).
45. Moss, P. The T cell immune response against SARS-CoV-2. *Nat Immunol* **23**, 186–193 (2022).
46. Koutsakos, M. *et al.* The magnitude and timing of recalled immunity after breakthrough infection is shaped by SARS-CoV-2 variants. *Immunity* **55**, 1316-1326.e4 (2022).
47. Koutsakos, M. *et al.* SARS-CoV-2 breakthrough infection induces rapid memory and de novo T cell responses. *Immunity* **56**, 879-892.e4 (2023).
48. Roychoudhury, P. *et al.* Tissue-resident T cell-derived cytokines eliminate herpes simplex virus-2-infected cells. *J Clin Invest* **130**, 2903–2919 (2020).
49. Schiffer, J. T. *et al.* Rapid localized spread and immunologic containment define Herpes simplex virus-2 reactivation in the human genital tract. *Elife* **2**, e00288 (2013).
50. Duke, E. R. *et al.* CMV viral load kinetics as surrogate endpoints after allogeneic transplantation. *J Clin Invest* **131**, (2021).
51. Li, J. *et al.* Age and Ebola viral load correlate with mortality and survival time in 288 Ebola virus disease patients. *Int J Infect Dis* **42**, 34–39 (2016).
52. Smith, C. L. & Stein, G. E. Viral load as a surrogate end point in HIV disease. *Ann Pharmacother* **36**, 280–7 (2002).
53. Krassenburg, L. A. P. *et al.* Evaluation of Sustained Virologic Response as a Relevant Surrogate Endpoint for Long-term Outcomes of Hepatitis C Virus Infection. *Clin Infect Dis* **72**, 780–786 (2021).
54. Fajnzylber, J. *et al.* SARS-CoV-2 viral load is associated with increased disease severity and mortality. *Nat Commun* **11**, 5493 (2020).
55. Westblade, L. F. *et al.* SARS-CoV-2 Viral Load Predicts Mortality in Patients with and without Cancer Who Are Hospitalized with COVID-19. *Cancer Cell* **38**, 661-671.e2 (2020).

56. Viloria Winnett, A. *et al.* Extreme differences in SARS-CoV-2 viral loads among respiratory specimen types during presumed pre-infectious and infectious periods. *PNAS nexus* **2**, pgad033 (2023).
57. Kissler, S. M. *et al.* Viral Dynamics of SARS-CoV-2 Variants in Vaccinated and Unvaccinated Persons. *N Engl J Med* **385**, 2489–2491 (2021).
58. Ortiz, M. E. *et al.* Heterogeneous expression of the SARS-Coronavirus-2 receptor ACE2 in the human respiratory tract. *EBioMedicine* **60**, (2020).
59. Hikmet, F. *et al.* The protein expression profile of ACE2 in human tissues. *Mol Syst Biol* **16**, (2020).
60. Ortiz Bezara, M. E. *et al.* Heterogeneous expression of the SARS-Coronavirus-2 receptor ACE2 1 in the human respiratory tract 2 3. doi:10.1101/2020.04.22.056127.
61. Wu, Y. *et al.* Incubation Period of COVID-19 Caused by Unique SARS-CoV-2 Strains: A Systematic Review and Meta-analysis. *JAMA Netw Open* **5**, e2228008 (2022).
62. Lindstrom, M. L. & Bates, D. M. Nonlinear mixed effects models for repeated measures data. *Biometrics* **46**, 673–87 (1990).

Figures

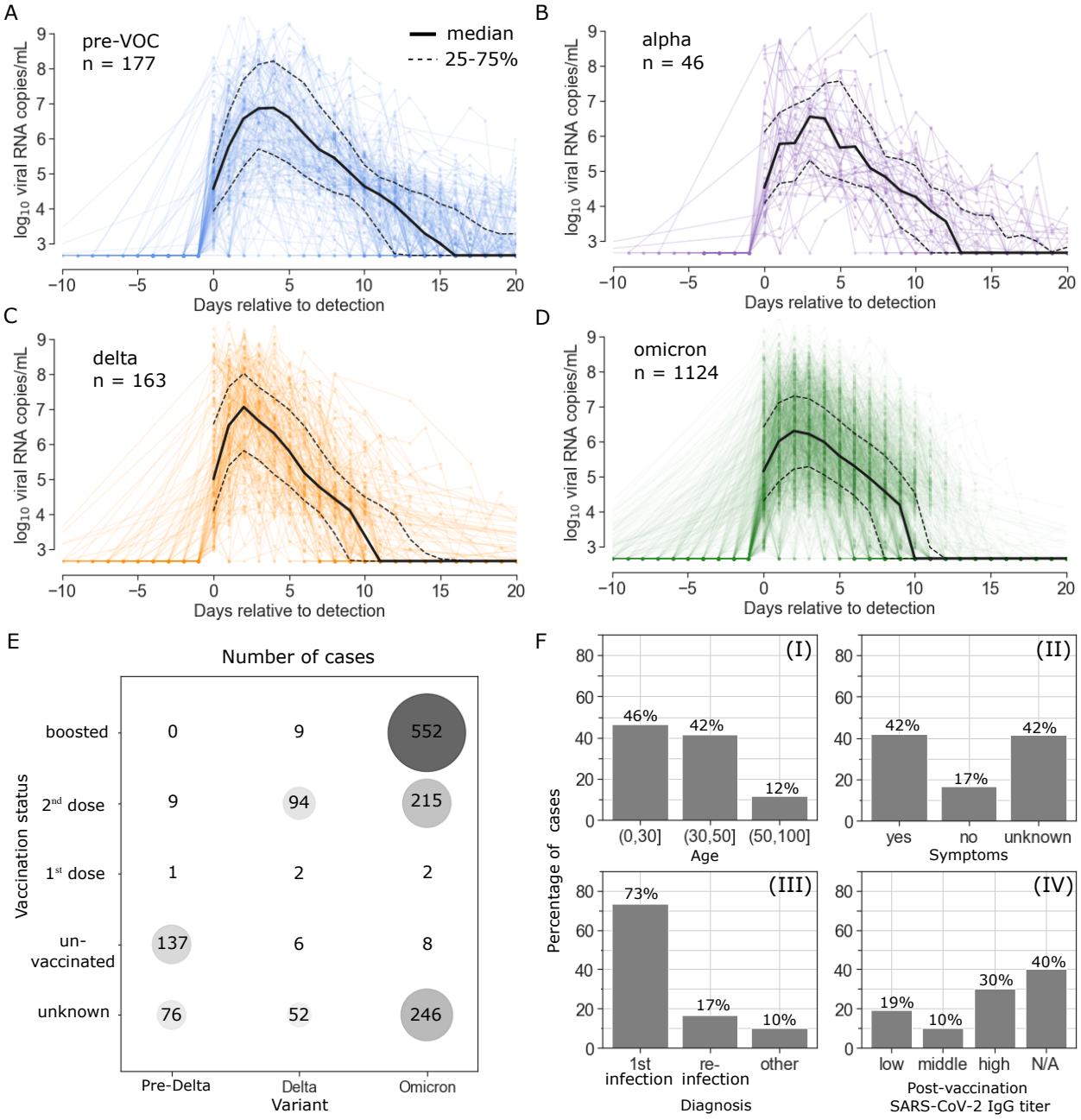

Figure 1: Viral kinetics by variant in the National Basketball Association cohort from June 2020-January 2022. *1510 SARS-CoV-2 infections are documented. Time series are stratified by variant with individual viral loads plotted in color, the median viral load plotted with a solid black line, and the 25th and 75th percentiles plotted in dashed black lines for (A) pre-variant of concern viruses, (B) alpha, (C) delta, and (D) omicron infections. (E) Bubble plot showing the correlation between variant of infection and vaccination status of the individual. Both the color and the size of the circle indicate the number of infections in each category. (F) Additional information about infections includes age, presence of symptoms, re-infection status, and pre-infection antibody titer following vaccination.*

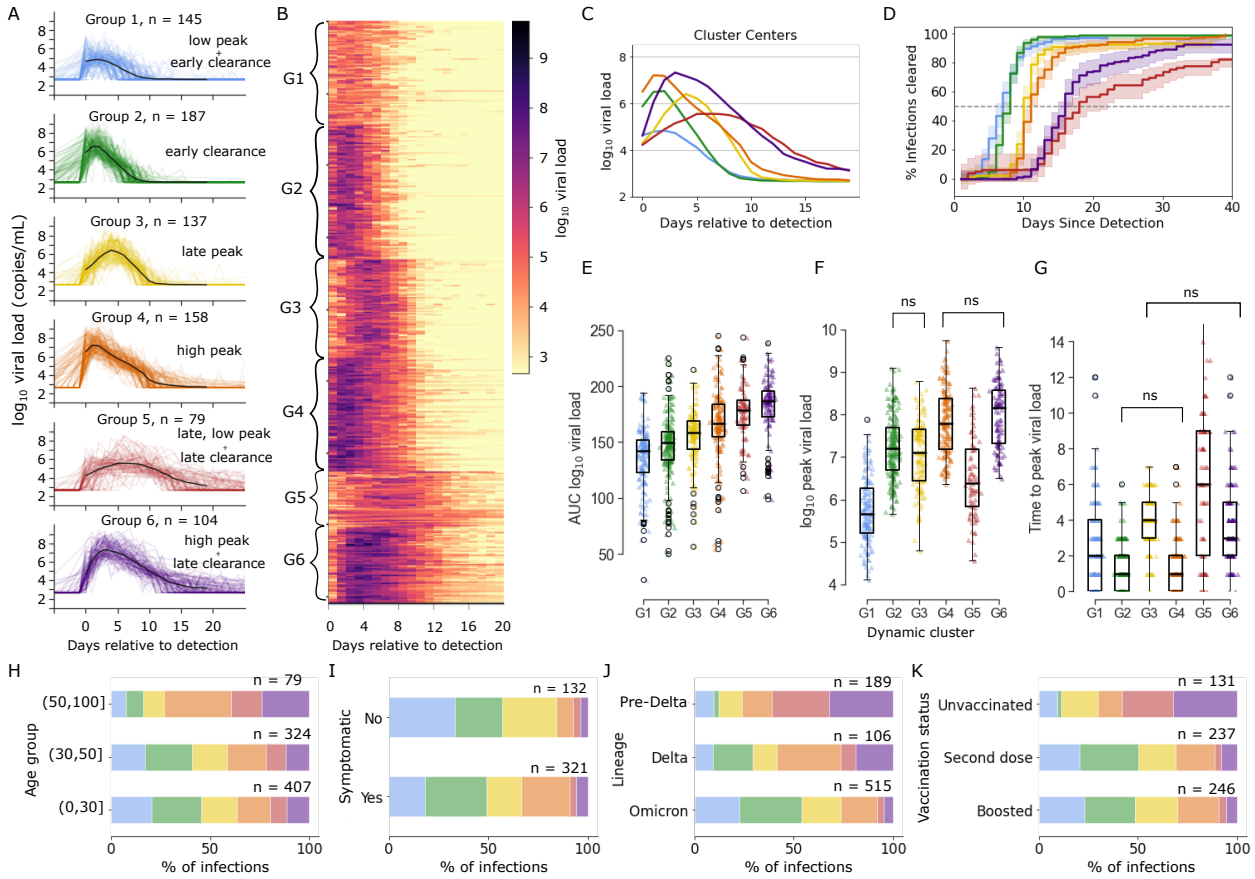

Figure 2: Distinct viral dynamic profiles in the National Basketball Association cohort from June 2020-January 2022. *(A) Trajectories stratified by cluster assignment after k-means clustering with k = 6. Cluster centers are shown in black. (B) Heat map of log viral load over time. Each row corresponds to an infection and trajectories are ordered according to cluster. (C) Cluster centers plotted on the same axis demonstrate differing peak viral loads, time of viral peak, clearance rate and time to clearance by cluster. (D) The proportion of infections cleared over time for each cluster with 95% confidence interval shaded. Boxplots of (E) area under the $\log_{10}$ viral load curve, (F) peak viral load for different dynamic groups, and (G) days between detection and peak vial load. According to a Mann-Whitney U-test, distinctions in the mean for all possible pairs of groups are significant ($p_{adjusted}$ < .05) except for the pairs marked "ns." In the final row, stacked bar charts indicate the percentage of cases that fall into each dynamic group when cases are stratified by (H) age group, (I) symptom status, (J) infecting variant, and (K) vaccination status.*

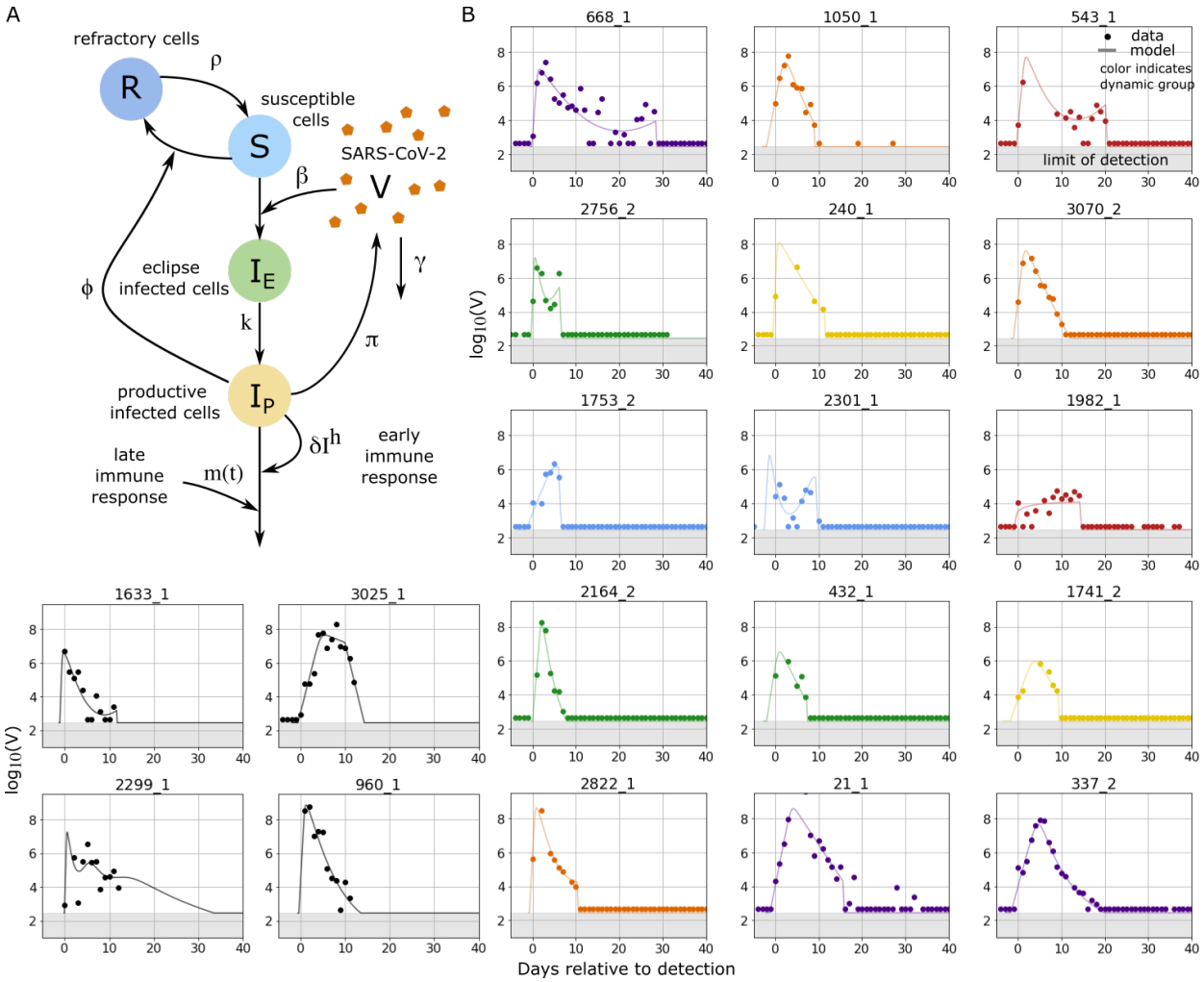

Figure 3: Mechanistic mathematical model with fits to viral loads from each cluster. *(A) Schematic of the ordinary differential equations model used to simulate SARS-CoV-2 infection with state variables indicated by capital letters, interactions indicated by arrows and parameters indicated by symbols adjacent to arrows. The model contains an early and late cytolytic immune response. (B) Examples of data from individual infections and corresponding model simulations colored according to cluster identified via k-means clustering as in* ***Fig 2*** *with group 1 in blue, group 2 in green, group 3 in yellow, group 4 in orange, and group 5 in red and group 6 in purple. The black examples were not included in cluster analysis. The model also captures instances of rebound or non-monotonic clearance.*

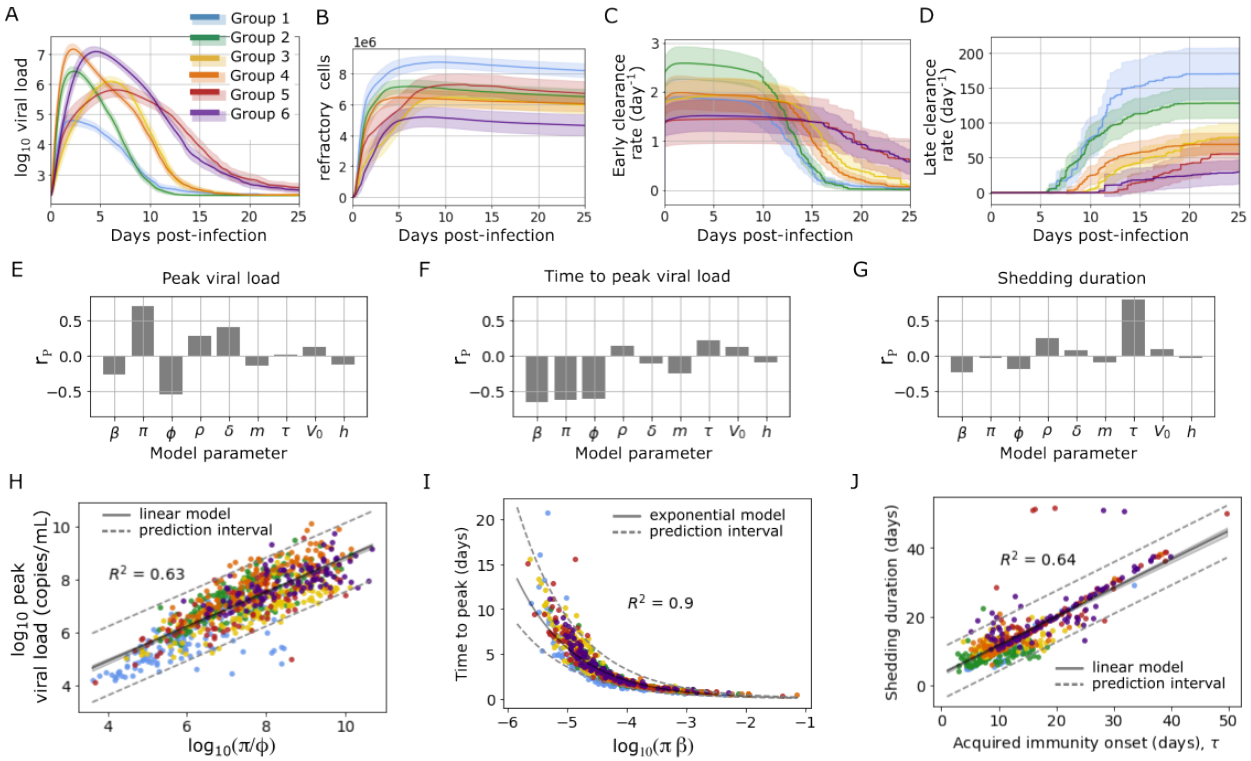

Figure 4: Mechanistic differences between dynamic groups. *Panels (A-D) show the mean of key quantities in the mechanistic model for each group over time with 95% confidence interval shaded. The quantities are (A) log viral load, $log_{10}(V)$, (B) number of cells that are refractory to infection likely due to interferon response, R, (C) early clearance rate of infected cells due to density-dependent, likely innate immune responses, δI^h, and (D) late clearance rate of infected cells likely due to acquired immune responses, $m(t)$. During persistent infection (G6), susceptible cells become refractory slowly, the early cytolytic responses are weak, and the late immune responses occur later and are less intense. Infections with high peak viral load that are cleared more rapidly (G2) have more rapid initial viral growth and more rapid and intense cytolytic immune responses relative to G6. Rapidly cleared, low viral load infections (G1) are notable for a rapid conversion of a larger portion of susceptible cells to a refractory state and a more rapid and potent acquired immune response. The Pearson correlation coefficient, r_p, between model parameters and kinetic quantities (E) peak viral load, (F) time to peak viral load, and (G) shedding duration provides insight into the sensitivity of model output to changes in parameters. (H) Peak height is largely explained by the ratio of the viral production rate over the rate of conversion of susceptible cells to a refractory state. (I) Time to peak viral load is largely explained by viral production rate and infectivity. (J) Shedding duration is largely explained by the time of activation of the acquired immune response.*

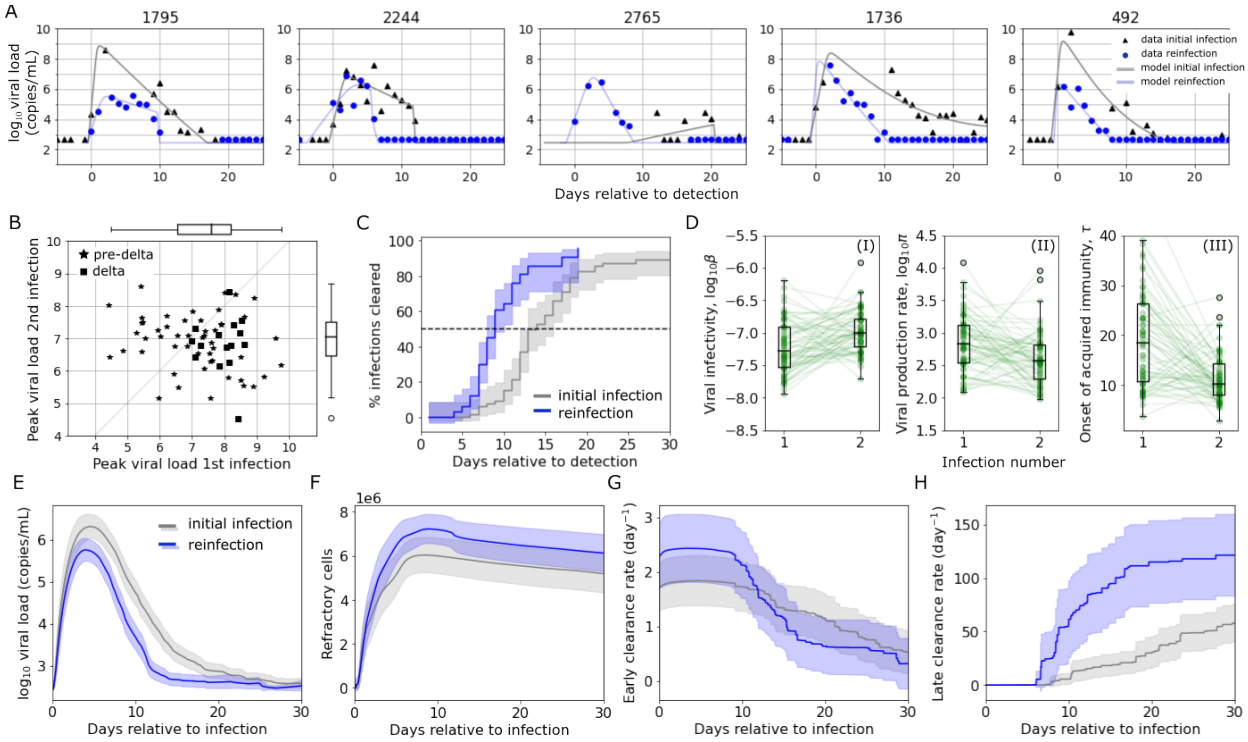

Figure 5: Mechanistic underpinning of more rapid clearance of SARS-CoV-2 during re-infection versus initial infection. *Initial infection and re-infection were documented for 67 individuals in the NBA cohort. (A) Examples of data and model fits for infection and reinfection in the same individual (B) As measured from the data, peak viral load of reinfection against peak viral load of first infection. In all cases the variant causing the reinfection was omicron, and the variant causing the first infection was either delta or a pre-delta variant. The mean peak viral load was around 0.5 log lower for second infection (t-test statistic = 2.26, p = .0254) (C) Proportion of infections cleared for reinfection (blue) and first infections (gray) over time, as measured from the data. Median time to clearance is 7.5 vs. 12 days since detection. (D) Boxplots of estimated individual parameters for infection and reinfection that are significantly different between the two groups ($p_{adjusted}$ < 0.05 for Mann-Whitney U-test). During re-infection with omicron, viral production was lower though infectivity was higher. The onset of the late immune response also occurs significantly earlier. (E) Mean viral load, (F) number of refractory cells, (G) early clearance rates, and (H) late clearance rates over time for the two groups as predicted by mechanistic model.*

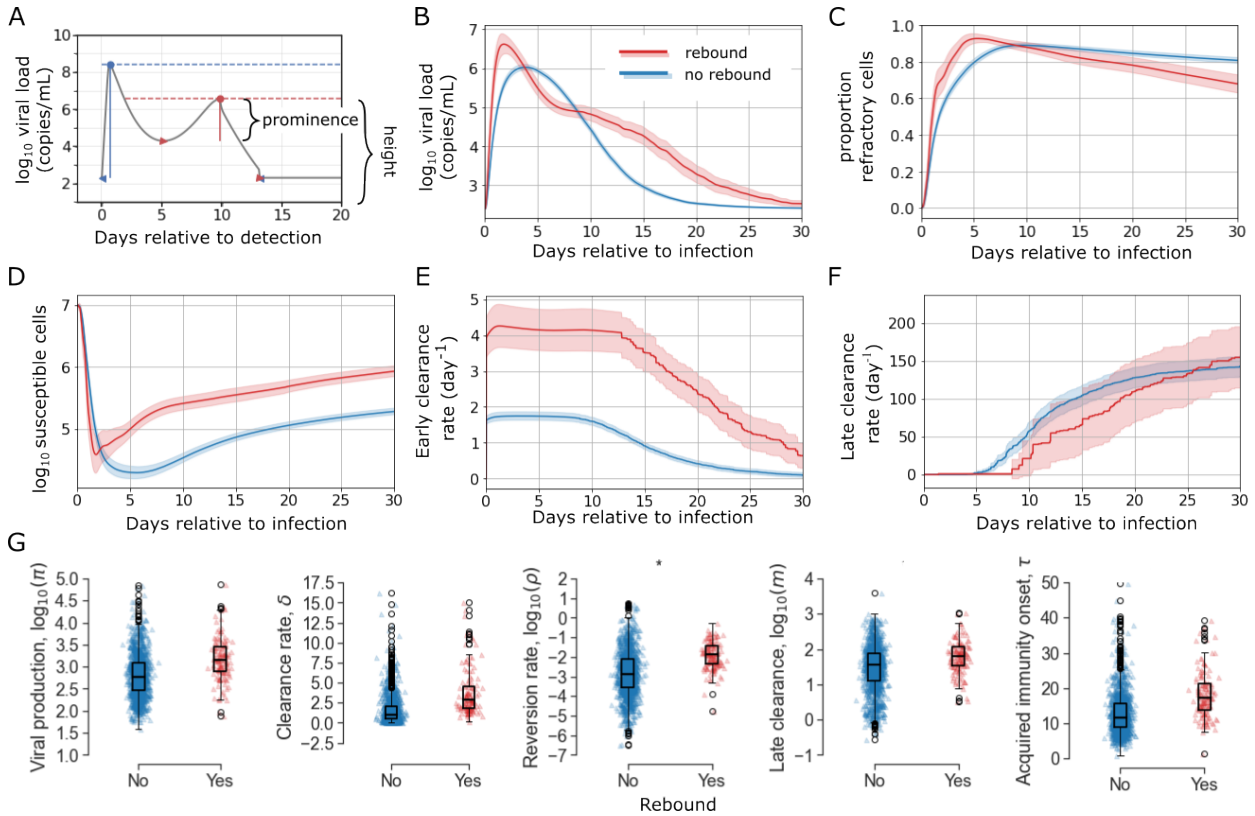

Figure 6: Model fitting to viral rebound in the NBA cohort. *(A) We classified infections as examples of viral rebound if there are at least two peaks in the model simulation with height of 4 logs and prominence of 1 log. Mean (B) viral load, (C) proportion of target cells that are refractory, (D) number of susceptible cells, (E) rate of early clearance, and (F) rate of late clearance as predicted by our mathematical model for rebound vs. non-rebound cases in red and blue respectively. 95% confidence interval shaded. (G) Distribution of individual parameter estimates for the rebound vs. non-rebound cases. Only those for which the mean differs significantly are displayed ($p_{adjusted}$ < .05 for Mann-Whitney U test).*